MATERIALS SCIENCE

Structurally integrated 3D carbon tube grid–based high-performance filter capacitor

Fangming Han[1]†, Ou Qian[1,2]†, Guowen Meng[1,2]*, Dou Lin[1,2], Gan Chen[1,2], Shiping Zhang[1,2], Qijun Pan[1,2], Xiang Zhang[1,2], Xiaoguang Zhu[1], Bingqing Wei[3]*

Filter capacitors play a critical role in ensuring the quality and reliability of electrical and electronic equipment. Aluminum electrolytic capacitors are the most commonly used but are the largest filtering components, limiting device miniaturization. The high areal and volumetric capacitance of electric double-layer capacitors should make them ideal miniaturized filter capacitors, but they are hindered by their slow frequency responses. We report the development of interconnected and structurally integrated carbon tube grid–based electric double-layer capacitors with high areal capacitance and rapid frequency response. These capacitors exhibit excellent line filtering of 120-hertz voltage signal and volumetric advantages under low-voltage operations for digital circuits, portable electronics, and electrical appliances. These findings provide a sound technological basis for developing electric double-layer capacitors for miniaturizing filter and power devices.

Filter capacitors play a critical role in ensuring the quality and reliability of electrical and electronic equipment, especially memory devices and computers (*1*, *2*). Circuit filtering has been dominated by aluminum electrolytic capacitors (AECs), which, unfortunately, are always the largest electronic component owing to their low volumetric capacitances (*1*, *3*, *4*). Therefore, developing new types of small-sized filter capacitors is vital to meet the current and emerging demands of digital circuits and portable electronics. The high areal and volumetric capacitance of electric double-layer capacitors (EDLCs) should make them an ideal candidate, but this is hindered by their slow frequency response (<1 Hz) (*2*, *5*, *6*). Miller *et al.* demonstrated the feasibility of using graphene-based EDLCs for circuit filtering (*1*). They revealed that the slow response of EDLCs could be modulated to meet the needs of circuit filtering applications by manipulating electrode materials and structures to enhance electrical and ionic conductivities.

EDLCs can be used in filter circuits to convert alternating current (ac) into direct current, however, they are required to have a high-frequency response to smooth the leftover ac ripples (*7*–*12*). The electrode materials must have superior electrical conductivity and fast ionic response to achieve rapid frequency performance (*13*). Additionally, the EDLCs are expected to have a high volumetric (C_V) and areal (C_A) specific capacitance. C_A is a more accurate evaluation index because the electrode thickness would be limited to ensure the rapid distribution of ions onto the inner surfaces to secure the high-frequency response. For a given capacitance, a low C_A will require increasing the active and inactive materials in the EDLC (*2*, *14*), resulting in a low C_V. Currently, EDLCs mainly use nanostructured carbon-based electrodes (*15*, *16*). To achieve a high-frequency response, such EDLCs can only use low loading of active materials, resulting in a subordinate C_A (*9*, *16*, *17*). This is because a high loading of active materials, such as graphene or carbon nanotube (CNT) arrays, tends to agglomerate into multilayer forms or bundles, leading to increased resistance to ion distribution and, hence, slow response (*18*, *19*). Although various approaches, such as using vertically structured and macroporous graphene, have been reported, these issues remain unresolved (*1*, *3*, *17*). Therefore, it is envisaged that a high-performance carbon-based filter EDLC electrode must have superior structural stability to maintain its high volumetric and areal capacitances and fast ion migration under operando conditions.

Here, we demonstrate the fabrication of high-performance line-filtering EDLCs using a three-dimensional (3D) carbon tube (CT) grid (3D-CTG) as the electrode. This grid, with truly interconnected and structurally integrated vertical and lateral CTs (denoted as 3D-CTs), can provide high structural stability, superior electrical conductivity, and an effective open porous structure and was synthesized by a chemical vapor deposition (CVD) method with the aid of a 3D interconnected nanoporous anodic aluminum oxide (3D-AAO) template (see materials and methods and figs. S1 and S2 in the supplementary materials) (*19*–*21*). The 3D-AAO template with lateral pores connecting the adjacent vertical channels was obtained by the anodization of Al foils with Cu impurity to form highly ordered vertically aligned nanochannels with Cu-contained nanoparticles embedded in the channel walls and subsequent selective wet-chemical etching of the nanoparticles (*20*, *21*). The 3D-CTs were constructed after growing CTs inside the 3D-AAO nanoporous template by pyrolyzing acetylene and removing the template. To increase the specific surface area and further enhance C_A, the 3D-CTs can be modified, as exemplified by filling with much-smaller-diameter CNTs within the vertical and lateral CTs (3D-CNT@CT) by means of the Ni catalyst–assisted CVD method (Fig. 1A) (*22*), or surface-treated with $KMnO_4$ (3D-RCT, i.e., 3D-CT with a rough surface) (fig. S3) (*23*).

The synthesized 3D-CTG film is flexible, with a diameter of 54 mm and a uniform thickness of 10 μm, and can be controlled using 3D-AAO templates of different sizes and thicknesses (Fig. 1B and fig. S4). Scanning electron microscopy (SEM) images reveal that the 3D-CTG films consist of uniformly distributed vertically aligned CTs, which are interconnected by smaller lateral CTs to form a 3D grid, and for 3D-CNT@CT, much-smaller-diameter CNTs were grown inside the vertical CTs (Fig. 1, C and D, and fig. S5). Transmission electron microscopy (TEM) images show that the vertical and lateral CTs are structurally integrated through chemical means rather than physical attachments (Fig. 1E and fig. S6). Moreover, the rough outer and inner surfaces of the 3D-RCT are also demonstrated (fig. S7).

EDLCs were assembled with two 3D-CTG electrodes of identical thickness [denoted as 3D-CT-10, 3D-CNT@CT-10, 3D-RCT-10, or 3D-RCT-12, where the numbers represent thickness (in micrometers)] separated by a nonwoven membrane with 1 M H_2SO_4 electrolyte (Fig. 2A). The Nyquist plot of the impedance obtained from the EDLCs (Fig. 2B) displays an imaginary response (Z'') almost vertical to the real axis, indicating a near-perfect capacitive characteristic and no porous electrode behavior (*1*, *24*, *25*). Also, no features are associated with the series of passive layers, characterized by the high-frequency semicircle (*1*, *25*). The Bode plots (frequency dependence of the phase angle) of the EDLCs and commercial AECs (Fig. 2C and fig. S8) were used to evaluate their frequency responses. An ideal EDLC should have a minimum phase angle of −90° (*1*). The 3D-CTG–based EDLCs and the commercial AEC can achieve phase angles of less than −80° when the frequency is <200 Hz. At a phase angle of −45°, the measured cutoff frequencies (f_{-45}; resistance and capacitive reactance are equal, defining the boundary between resistive and capacitive behavior) of 3D-CT-10–, 3D-CNT@CT-10–, and 3D-RCT-10–based EDLCs and the commercial AEC are 2634, 2360, 1332, and

[1]Key Laboratory of Materials Physics and Anhui Key Laboratory of Nanomaterials and Nanotechnology, Institute of Solid State Physics, Hefei Institutes of Physical Science, Chinese Academy of Sciences, Hefei 230031, China. [2]Department of Materials Science and Engineering, University of Science and Technology of China, Hefei 230026, China. [3]Department of Mechanical Engineering, University of Delaware, Newark, DE 19716, USA.
*Corresponding author. Email: gwmeng@issp.ac.cn (G.M.); weib@udel.edu (B.W.)
†These authors contributed equally to this work.

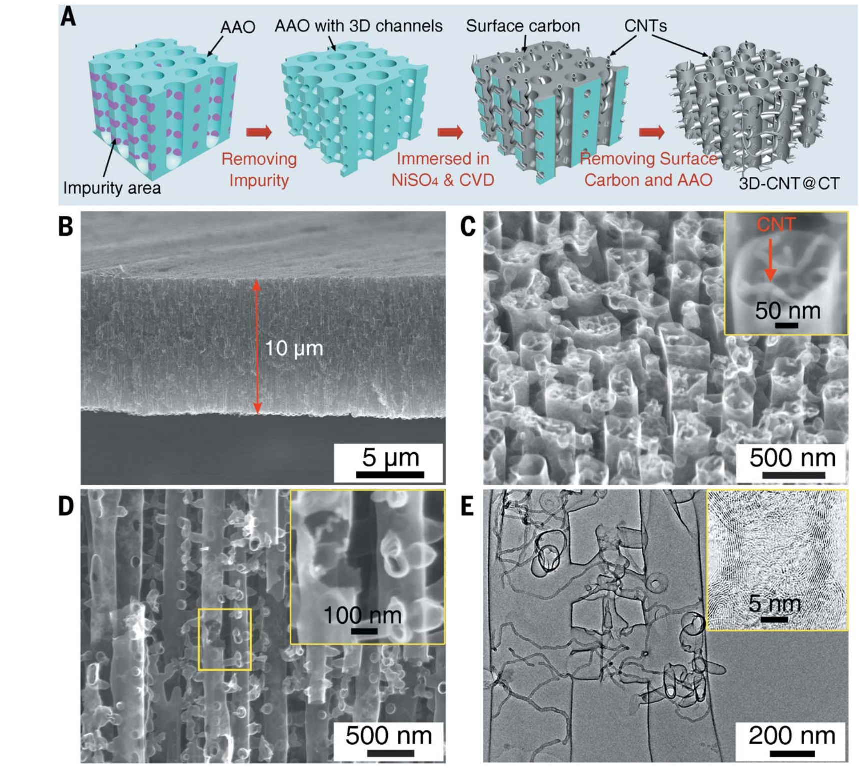

Fig. 1. Synthesis and characteristics of the 3D-CNT@CT grid. (**A**) Schematic illustration of synthetic procedures of the 3D-CNT@CT grid. (**B**) Typical cross-sectional view, (**C**) top view, and (**D**) enlarged cross-sectional view SEM images of 3D-CNT@CT. (Insets) High-magnification SEM images. (**E**) High-resolution TEM image of two adjacent vertical CTs connected by lateral CTs with filling CNTs. (Inset) Magnified TEM image of a CNT.

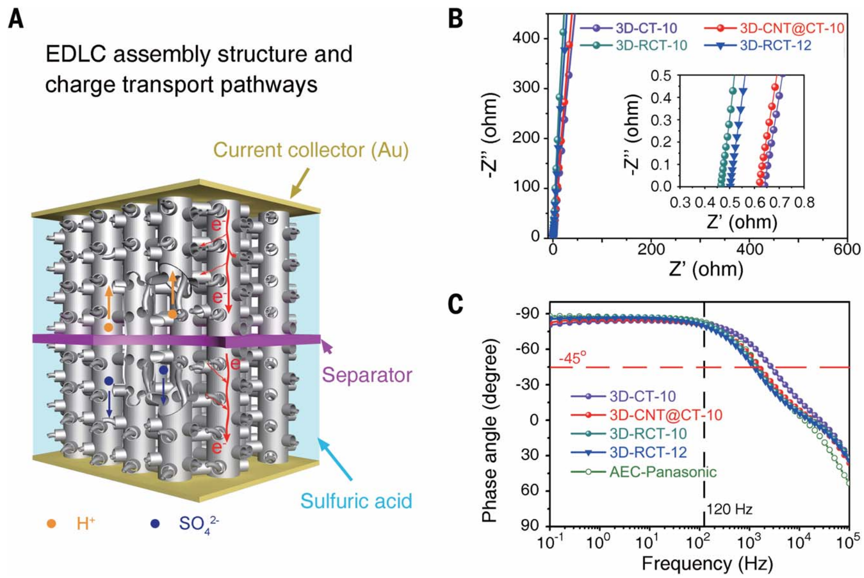

Fig. 2. Assembly structure and electrochemical impedance spectra of the 3D-CTG capacitor. (**A**) Schematic of EDLC assembly structure. (**B**) Complex plane plot of the 3D-CTG–based EDLCs. (**C**) Phase angle versus frequency of 3D-CT-10–, 3D-CNT@CT-10–, 3D-RCT-10–, and 3D-RCT-12–based EDLCs and commercial AEC (Panasonic, Japan, 6.3 V/330 μF).

1502 Hz, respectively. These results demonstrate that the EDLCs built with 3D-CTGs have frequency responses similar to that of the commercial AEC. A low phase angle at 120 Hz is a vital indicator for practical applications of EDLCs as ac line-filtering capacitors. This angle is lower than −81° for the 3D-CTG–based EDLCs, similar to the phase angle of the commercial AEC (−83°, Panasonic Japan, 330 μF, 6.3 V). The excellent and stable ac line-filtering performance is also demonstrated (fig. S9).

The frequency dependences of the areal and volumetric capacitances (Fig. 3, A and B) prove that the 3D-CTG–based EDLCs can deliver much higher capacitances at all frequencies than those of AECs, and only slightly decreased capacitances were observed when the frequency increased from 10^{-1} to 10^{3} Hz. The C_A of the 3D-RCT-12–based EDLCs can reach 2.81 mF cm^{-2} at 120 Hz, a higher areal-specific capacitance than that of other filtering EDLCs reported to date with a phase angle less than −80° (Fig. 3C and table S1) (*1*, *5*, *7*–*9*, *11*, *13*, *16*, *26*, *27*). The C_V at 120 Hz can achieve 1.36 F cm^{-3} for 3D-RCT-10 electrodes. These excellent performances—showing the enhancement of structural stability, endorsement of electrical conductivity, and improvement of ion response—illustrate the superiority of the truly interconnected and structurally integrated 3D-CTGs.

To meet the voltage requirements of the ac line filtering, taking the 6.3-V AEC as a benchmark, six EDLCs based on the 1.4-cm-diameter 3D-CT electrodes were assembled in series (fig. S10). The EDLCs in series also show ideal capacitive behavior (fig. S11). To eliminate the influence of the contact resistance, a four-electrode test method was used to evaluate the electrochemical impedance spectroscopy of the EDLCs. Complex plane plots of a single EDLC and the six-EDLC series (Fig. 4A) exhibit close to 90° slopes at a high frequency, which is also characteristic of a pronounced capacitive behavior. Typically, the increase of equivalent series resistance (ESR) caused by capacitors in series would theoretically lead to the degradation of frequency response performance. However, the curves of a single device and the six EDLCs in series showing the frequency dependence of the phase angle in the Bode plots almost exactly overlap below 10^4 Hz (Fig. 4B), and the phase angle at 120 Hz reaches −82°, suggesting that the sixfold increase of ESR does not slow the frequency response. This is mainly because the rise of ESR is accompanied by a corresponding augmentation in capacitive reactance (X_c) (table S2), which would result in high-voltage line-filtering EDLCs.

In the complex model of the capacitance (Fig. 4C), $C'(f)$ represents the accessible capacitance at the corresponding frequency, while $C''(f)$ accounts for energy dissipation due to irreversible processes caused by the diffusion and polarization (*28*). The 3D CT array structure allows high capacitance to be maintained to frequencies exceeding 120 Hz, and the capacitance of a single EDLC is almost six times that of the six EDLCs in series, which is consistent with the law of capacitors in series. Especially for the single EDLC and six EDLCs in series, $C''(f)$ goes through maximum values at the same

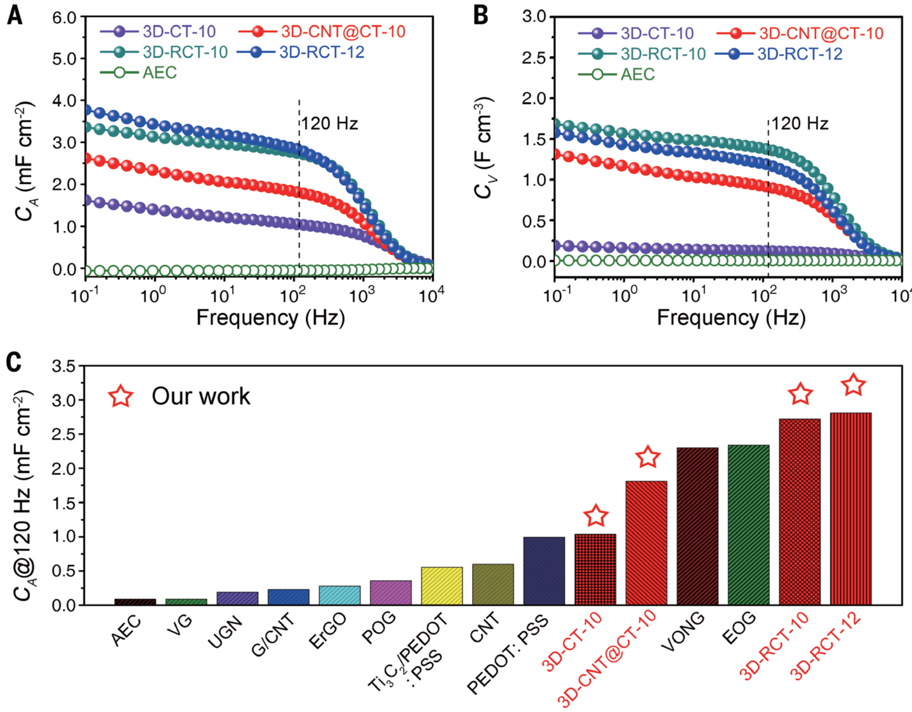

Fig. 3. Frequency-dependent capacitances of 3D-CTG–based EDLCs. (**A** and **B**) C_A and C_V versus frequency of 3D-CT-10–, 3D-CNT@CT-10–, 3D-RCT-10–, and 3D-RCT-12–based EDLCs and commercial AEC. (**C**) Comparison of the C_A at 120 Hz of 3D-CT-10–, 3D-CNT@CT-10–, 3D-RCT-10–, and 3D-RCT-12–based EDLCs and other reported electrochemical capacitors used in the ac filter circuits with the phase angle near or less than −80°. The abbreviations and corresponding phase angles in (C) are as follows: AEC (Panasonic, −83°); VG (vertical graphene, −82°) (*1*); UGN (unzipped graphene nanoribbons, −85°) (*9*); G/CNT (grapheme/CNT, −81.5°) (*15*); ErGO (electrochemical reduction of graphene oxide, −84°) (*7*); POG (perpendicularly oriented graphene, −82°) (*5*); Ti_3C_2/PEDOT:PSS [Ti_3C_2/poly(3,4-ethylenedioxythiophene): poly(styrenesulfonate), −79°] (*13*); CNT (−81°) (*16*); PEDOT:PSS [poly(3,4-ethylenedioxythiophene): poly(styrenesulfonate), −83.6°] (*8*); VOGN (vertically oriented graphene nanosheets, −85°) (*11*); and EOG (edge-oriented graphene, −80.6°) (*27*).

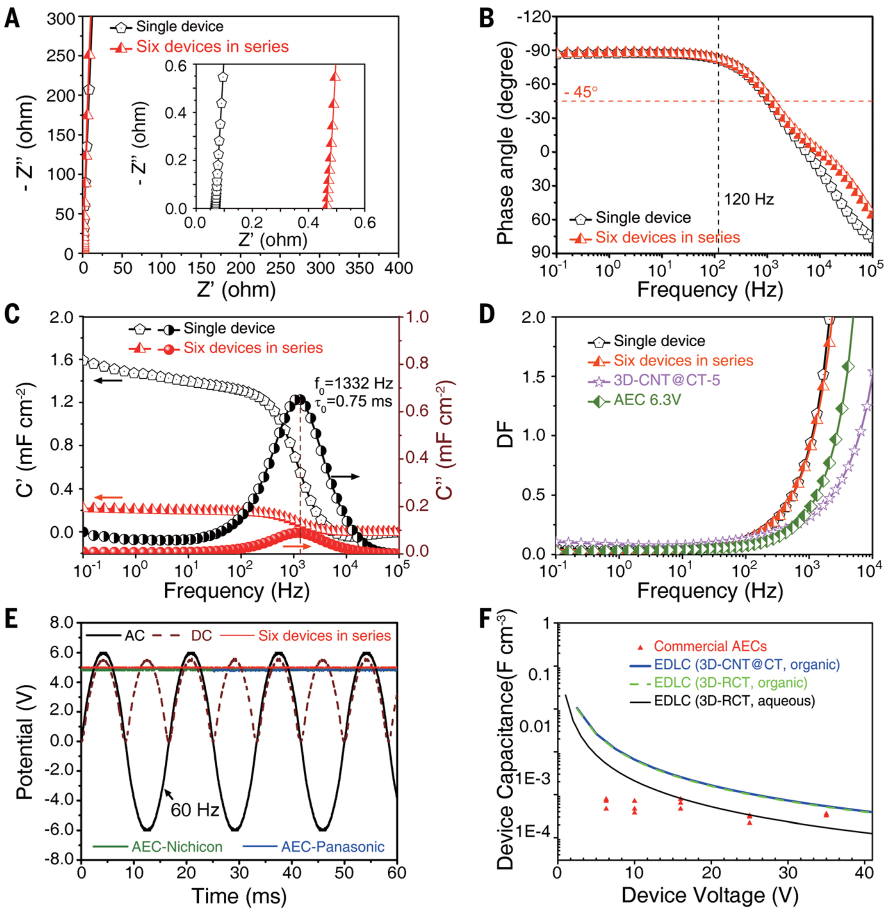

Fig. 4. Performance characteristics of single EDLC and EDLCs in series. (**A**) Nyquist plots. (**B**) Phase angle versus frequency. (**C**) Real and imaginary parts of capacitance versus frequency. (**D**) DF versus frequency. (**E**) Filtering results of the six EDLCs in series in comparison with AECs. (**F**) A volumetric comparison of 3D-CTG–electrode EDLCs with commercial AECs (red triangles; Panasonic, Nichicon, and Nippon, Japan).

frequency, f_0, defining a time constant as $\tau_0 = 1/f_0 = 0.75$ ms, which further confirms that high-performance and high-voltage filtering capacitors can be achieved by connecting EDLCs in series.

In addition, the high-frequency response can also be demonstrated by the variation of C'/C and dissipation factors (DFs) with frequency. The C'/C value approaches 1 below a kilohertz (fig. S11C), indicating the ideal capacitive behavior in this frequency range. The DFs have a very small value at 120 Hz (Fig. 4D), suggesting a slight loss characteristic of the devices. Although there is still a gap with an AEC, a smaller DF can be achieved by adjusting the thickness of the 3D-CTG. More critically, the EDLCs in series also exhibit excellent ac line-filtering performance (Fig. 4E), and the ripple current is ~0.014 A at 120 Hz (calculations given in the supplementary materials).

It is critical to compare the volume of the EDLCs to the comparably rated AECs (Fig. 4F and fig. S12). The calculated capacitance per volume (C_V, in farads per cubic centimeter) for the exemplified 3D-RCT–based EDLC in the aqueous electrolyte is $0.21/V^2$, where V is the voltage rating (all components included). The volumetric capacitances are much higher than a commercial AEC when the operation voltage is below ~10 V. To increase operating voltages, the organic electrolyte (tetraethylammonium tetrafluoroborate in acetonitrile) was used (figs. S13 and S14; calculations given in the supplementary materials). The volumetric capacitance to rated voltage increases to $0.66/V^2$, and then volumetric advantages over an AEC are expanded to voltages below

~25 V, exhibiting considerable advantages in low-voltage operations for digital circuits, portable electronics, and small appliances and meeting the roadmap of low operating voltage in high-performance devices and systems (*29*). The comparison of CV/v value (the amount of electric charge stored per volume, V is voltage, and v is volume) shows a similar result (fig. S15). It should be noted that given the low operation voltage of an individual EDLC, more EDLCs must be connected in series to reach a higher-rated voltage. Further optimization to achieve volumetric advantages at higher voltages is also possible through applying in-plane interdigitated electrode configuration and using solid or ionic electrolytes (*25*, *30*). The developed 3D-CTG–based EDLCs to replace the bulky AECs would benefit the miniaturization of portable electronics, mobile power supply, electrical appliances, and distributed energy harvesting and power supply on the Internet of Things, greatly promoting the development of high-performance digital circuits and emerging electronic technologies.

In this study, we have successfully synthesized freestanding thin films with 3D truly interconnected, structurally integrated CT grids. The freestanding thin films of 3D-CT, 3D-CNT@CT, and 3D-RCT have been innovatively used to fabricate EDLCs with demonstrated effectiveness to resolve the critical bottleneck issues of slow frequency response of the existing carbon-based EDLCs as ac line-filtering capacitors and the low C_A and C_V faced by commercial AECs. These encouraging results pave the way for the miniaturization of filtering capacitors with high capacitance using carbon-based electrodes, which is essential for current and emerging portable electronics.

REFERENCES AND NOTES

1. J. R. Miller, R. A. Outlaw, B. C. Holloway, *Science* **329**, 1637–1639 (2010).
2. Z. Y. Fan, N. Islam, S. B. Bayne, *Nano Energy* **39**, 306–320 (2017).
3. F. Y. Chi *et al.*, *Adv. Energy Mater.* **7**, 1700591 (2017).
4. K. U. Laszczyk *et al.*, *Adv. Energy Mater.* **5**, 1500741 (2015).
5. G. F. Ren, X. Pan, S. Bayne, Z. Y. Fan, *Carbon* **71**, 94–101 (2014).
6. M. F. El-Kady, V. Strong, S. Dubin, R. B. Kaner, *Science* **335**, 1326–1330 (2012).
7. K. Sheng, Y. Sun, C. Li, W. Yuan, G. Shi, *Sci. Rep.* **2**, 247 (2012).
8. M. Zhang *et al.*, *Energy Environ. Sci.* **9**, 2005–2010 (2016).
9. J. Lim *et al.*, *Nat. Commun.* **7**, 10364 (2016).
10. L. Huang, L. Dai, *Angew. Chem. Int. Ed.* **56**, 6381–6383 (2017).
11. D. Premathilake *et al.*, *J. Electrochem. Soc.* **165**, A924–A931 (2018).
12. M. Wu *et al.*, *Nat. Commun.* **10**, 2855 (2019).
13. G. S. Gund *et al.*, *Joule* **3**, 164–176 (2019).
14. N. A. Kyeremateng, T. Brousse, D. Pech, *Nat. Nanotechnol.* **12**, 7–15 (2017).
15. J. Lin *et al.*, *Nano Lett.* **13**, 72–78 (2013).
16. Y. Rangom, X. S. Tang, L. F. Nazar, *ACS Nano* **9**, 7248–7255 (2015).
17. D. Premathilake, R. A. Outlaw, S. G. Parler, S. M. Butler, J. R. Miller, *Carbon* **111**, 231–237 (2017).
18. H. Sun *et al.*, *Science* **356**, 599–604 (2017).
19. M. Tian *et al.*, *Nano Energy* **11**, 500–509 (2015).
20. I. S. Molchan, T. V. Molchan, N. V. Gaponenko, P. Skeldon, G. E. Thompson, *Electrochem. Commun.* **12**, 693–696 (2010).
21. J. Vanpaemel, A. M. Abd-Elnaiem, S. De Gendt, P. M. Vereecken, *J. Phys. Chem. C* **119**, 2105–2112 (2015).
22. J. Shi, Y. F. Lu, K. F. Tan, X. W. Wang, *J. Appl. Phys.* **99**, 024312 (2006).
23. G. Wang *et al.*, *Adv. Mater.* **26**, 2676–2682 (2014).
24. Z. S. Wu, Z. Liu, K. Parvez, X. Feng, K. Müllen, *Adv. Mater.* **27**, 3669–3675 (2015).
25. J. R. Miller, R. A. Outlaw, *J. Electrochem. Soc.* **162**, A5077–A5082 (2015).
26. N. Islam *et al.*, *Nano Energy* **40**, 107–114 (2017).
27. W. Y. Li, S. Azam, G. Z. Dai, Z. Y. Fan, *Energy Storage Mater.* **32**, 30–36 (2020).
28. C. G. Zhang, H. Z. Du, K. Ma, Z. H. Yuan, *Adv. Energy Mater.* **10**, 2002132 (2020).
29. Institute for Electrical and Electronics Engineers (IEEE), "International roadmap for devices and systems (IRDS): Beyond CMOS, 2021 Update" (IEEE, 2021); https://irds.ieee.org/images/files/pdf/2021/2021IRDS_BC.pdf.
30. M. F. El-Kady, R. B. Kaner, *Nat. Commun.* **4**, 1475 (2013).

ACKNOWLEDGMENTS

The authors are grateful to P. M. Ajayan from Rice University and H. J. Zhao from Griffith University for helpful discussion. **Funding:** Funding was provided by Natural Science Foundation of China grant 91963202 (G.M.); Natural Science Foundation of China grant 52072372 (F.H.); Key Research Program of Frontier Sciences, CAS grant QYZDJ-SSW-SLH046 (G.M.); CAS/SAFEA International Partnership Program for Creative Research Teams (G.M.); and Hefei Institutes of Physical Science, Chinese Academy of Sciences Director's Fund grant YZJJZX202018 (F.H.). **Author contributions:** Conceptualization: F.H., O.Q., G.M., and B.W. Methodology: F.H., O.Q., G.M., B.W., and X.Zhu. Investigation: F.H., O.Q., D.L., G.C., S.Z., Q.P., X.Zhang, and X.Zhu. Visualization: F.H., O.Q., D.L., G.C., S.Z., Q.P., and X.Zhang. Funding acquisition: G.M. and F.H. Project administration: G.M., B.W., and F.H. Supervision: G.M. and B.W. Writing – original draft: F.H. and O.Q. Writing – review & editing: G.M., B.W., F.H., and O.Q. **Competing interests:** The authors declare that they have no competing interests. **Data and materials availability:** All data are available in the main text or the supplementary materials.

SUPPLEMENTARY MATERIALS

science.org/doi/10.1126/science.abh4380
Materials and Methods
Supplementary Text
Figs. S1 to S15
Tables S1 and S2
References (*31*–*47*)

Submitted 9 March 2021; resubmitted 14 April 2022
Accepted 22 July 2022
10.1126/science.abh4380

Science

Structurally integrated 3D carbon tube grid–based high-performance filter capacitor

Fangming HanOu QianGuowen MengDou LinGan ChenShiping ZhangQijun PanXiang ZhangXiaoguang ZhuBingqing Wei

Science, 377 (6609), • DOI: 10.1126/science.abh4380

Carbon-based filter capacitors
Filter capacitors are used in filter circuits to convert alternating current into direct current by smoothing out ripples in the incoming supply. They have been dominated by aluminum electrolytic capacitors and are typically the largest component in an electronic circuit because of their low areal capacitances, thus limiting the potential for miniaturization. Using three-dimensional porous anodic aluminum oxide (AAO) templates, Han *et al*. constructed a network of carbon tubes in which they deposited nickel catalyst nanoparticles and grew vertically aligned carbon nanotubes using chemical vapor deposition. After removal of the AAO, a flexible film was obtained. The films showed a 25% improvement in areal capacitance at 120 hertz and can be connected in series without affecting their electrochemical performance. —MSL